Article

Intrinsically soft and fully recyclable robotic sensors with quadruple sensing functions for reliable human-robot interactions

Yuexin Cao [a,1], Yuxiang Peng [a,1], Wenjuan Ren [a,1], Honghao Wang [a], Yan Diao [a], Zhimeng Liu [b,*], Xin He [b], Hua Luo [a], Xiaodong Wu [a,*]

[a] School of Mechanical Engineering, Sichuan University, Chengdu 610065, China
[b] School of Chemical Engineering, Sichuan University, Chengdu 610065, China

ARTICLE INFO

ABSTRACT

Human-robot interaction (HRI) is becoming ubiquitous where both humans and robots perform tasks, while reliable robotic sensors are the prerequisite for efficient and safe HRI, especially in unstructured or dynamic environments. A wide spectrum of robotic sensors has been developed but most of them are limited to single or dual functionality, making it challenging to perceive complex environments. Here, we present a type of intrinsically soft robotic sensor with quadruple sensing functionalities integrated into a single device, including spatial approach sensing, thermal approach sensing, thermal touch sensing, and mechanical force sensing. Through such quadruple sensing functions, both thermal and mechanical stimulations can be well resolved in both contact and non-contact manners. More importantly, all components of the robotic sensors can be fully recycled for reuse upon the sensor's end of service, achieving superior cost-efficiency and eco-sustainability. As demonstrations, a close-loop intelligent HRI system is constructed via integrating our intrinsically soft sensors with pneumatic soft grippers and programmable robotic arms. A diversity of reliable HRI scenarios (e.g., human-robot interfacing, object perception/classification, bedside clinical care, etc.) are successfully demonstrated leveraging the quadruple sensing functionalities. This study presents a new path to enrich robotic sensing functionality and enhance HRI reliability in complex environments.

1. Introduction

With the rapid development of smart robotics and artificial intelligence, human-robot interaction (HRI) is becoming ubiquitous or even inevitable in the fields of advanced manufacturing, medical diagnosis and treatment, smart homes, entertainment, logistics industry, and service industry [1–5]. Safe and efficient HRI, especially in dynamic and uncertain environments, is highly desired for adaptive mobility, physical manipulation, or social interaction, while robotic sensors are the key to enabling reliable HRI.

In the past decades, a wide spectrum of robotic sensors has been developed to perceive external environment and detect various parameters [6–9]. Particularly, flexible and soft robotic sensors have attracted numerous attentions due to their superior conformability to three-dimensionally curved surfaces or dynamically varying surfaces, with higher accuracy and reliability compared to their rigid counterparts. Diverse parameters can be detected with flexible robotic sensors, including pressure [10,11], temperature [12,13], proximity [14–16], and other environmental factors [5,17]. For example, flexible pressure sensors could be used to resolve the magnitudes and distributions of mechanical stimuli, thereby assisting the robots to manipulate objects safely and delicately. Flexible temperature sensors can endow the robots with the ability to perceive the environment temperature or object temperature. Flexible proximity sensors can detect the approaching of external objects, avoiding dangerous collisions with human body or obstacles. Nevertheless, the vast majority of the developed flexible robotic sensors have a single functionality and cannot be used to resolve complex environmental information.

Recently, multifunctional robotic sensors with different sensing capabilities have been developed and exhibit great potential for HRI application [18–27]. For instance, flexible robotic sensors

capable of detecting both static and dynamic mechanical stimulations are demonstrated by integrating piezoresistive sensing elements with triboelectric or piezoelectric sensing elements [18,19]. In addition, flexible robotic sensors that can resolve both mechanical stimuli and thermal stimuli based on different sensing mechanisms (e.g., piezoresistive and thermoelectric) have been fabricated [20,21]. Moreover, bimodal robotic sensors for detecting the proximity of external objects and the subsequent applied pressure have been realized based on capacitive sensing mechanism [22–24]. These pioneering works extend and enrich the functionality of conventional robotic sensors, and enable robots to interact with the surroundings in a more precise, rapid, and safe manner. However, despite the significant advancements made recently, most of the reported multifunctional robotic sensors are limited to dual-functional integration. Monolithic and seamless integration of more complex functionalities into a single device for reliable HRI still remains challenging [28–32].

Here, inspired by natural skin's sensing capabilities, we present a new class of intrinsically soft robotic sensors with quadruple sensing functionalities integrated into a single device (Fig. 1a), including spatial approach sensing, thermal approach sensing, thermal touch sensing, and mechanical force sensing. With such versatility, both mechanical and thermal stimulations could be well resolved through both contact and non-contact modes (Fig. 1b and c). The fabricated robotic sensors possess good flexibility and intrinsic softness (Fig. 1d), enabling them to conformally adapt to complex 3D curved surfaces. More importantly, all the ingredients of the robotic sensors can be fully recycled and reused to construct new batches of sensors (Fig. 1e), significantly alleviating the resource consumption problem and the environmental hazards caused by electronic waste. As proof-of-concept demonstrations, a close-loop and reliable HRI system is built by integrating the robotic sensors onto a soft gripper and a robotic arm. A diversity of reliable HRI scenarios (e.g., human-robot interaction, object perception and classification, bedside clinical care, etc.) are successfully demonstrated by leveraging the quadruple sensing functions. This study provides a feasible and versatile platform for comprehensive robotic sensations.

2. Experimental

2.1. Materials

Polyvinyl Alcohol (PVA, 1788) was purchased from Kelong Chemical Reagent Co. Ltd. (China). Ionic liquid (IL) of 1-Ethyl-3-Methylimidazolium Bis (Trifluoromethyl sulfonyl) Imide ([EMIM]$^+$[TFSI]$^-$) was provided from Adamas Reagent Co. Ltd. (Shanghai, China). Conductive silver ink (CI-1036) was purchased from Engineered Materials Solutions (EMS), Inc. (USA). The Polytetrafluoroethylene (PTFE) molds were provided by Yixing Experimental Equipment Co. Ltd. (China). TPU films were purchased from Zhibiyou Materials Ltd. (China). Polytetramethylene glycol (PTMG, Mn = 2000 g/mol) was purchased from Mitsubishi Chemical Industries, Ltd. (Japan). Dimethylolpropionic acid (DMPA, AR), and isophorone diisicyanate (IPDI, 99.5%) were obtained from Shanghai Titan Scientific Co. Ltd. (China). Trimethylolpropane polyethylene glycol monomethyl ether (Ymer N120, reagent grade, Mn = 1000) was obtained from Perstorp in Sweden. Triethylamine (TEA, AR), ethylenediamine (EDA, AR), and N,N-dimethylformamide (DMF, AR) were purchased from Chengdu Kelong Chemical Reagent Co. Ltd. (China). Before use, the PTMG and Ymer N120 were vacuumdried at 110 °C for 2 h.

2.2. Synthesis of ethanol-soluble polyurethane (ES-PU)

The synthetic route of ES-PU is shown in Fig. S1 (online). Firstly, 100 g (0.05 mol) PTMG, 3.5 g (0.0035 mol) Ymer N120, 3.5 g (0.026 mol) DMPA, 26.5 g (0.119 mol) IPDI, and 30 g DMF were added into a three-round bottom flask with an overhead stirrer and reacted at 80 °C for 12 h to obtain prepolymer. Secondly, the prepolymer was cooled to 40 °C, and the 2.64 g (0.026 mol) TEA was added to neutralize the carboxyl in DMPA. Afterwards, the deionized water was gradually introduced into the prepolymer under stirring to obtain the waterborne prepolymer dispersion. Finally, the dispersion was cooled to 25 °C, and an EDA aqueous solution, prepared by mixing 2.60 g (0.043 mol) EDA with 30 g deionized water, was dropwise added into the dispersion under continuous agitation within 30 min, followed by further stirring for 1 h to complete the chain extension and obtain the ES-PU emulsion.

2.3. Printing of Ag electrode patterns on TPU substrate

The printing process of Ag electrode patterns on TPU substrate is shown in Fig. S2a (online). The interdigital Ag electrodes were printed on commercial TPU film via screen-printing method. First, a self-designed screen-mesh with specific patterns was placed on the TPU substrate, and elastic conductive Ag paste was applied onto the screen-mesh, followed by spreading the Ag paste uniformly with rubber squeegee. At last, the Ag electrodes printed on TPU substrate was placed in an oven at 65 °C for 1 h to cure the Ag paste.

### 2.4. Fabrication of the ionic temperature sensing layer

The fabrication of the ion temperature sensing layer is shown in Fig. S2b (online). First, PVA powders were dissolved in deionized water via magnetically stirring at 80 °C for 3 h to obtain an aqueous PVA solution (10 wt%). Secondly, a certain amount of IL was mixed with the PVA solution and the weight ratio of PVA:IL is 4:1. The well-mixed PVA/IL solution was casted into a flat PTFE mold, followed by drying in oven at 65 °C for 1.5 h. At last, the cured film was peeled off from the PTFE mold and cut into self-defined shape via laser cutting for later use.

2.5. Fabrication of the ES-PU insulation layer

Fabrication of the ES-PU insulation layer is shown in Fig. S2c (online). Specific amount of ES-PU solution (29 wt%) was poured into a flat PTFE mold and dried at room temperature for about 2 d until the ES-PU solution completely solidified into a film. The ES-PU film was peeled off carefully and then cut into specific shape and size via laser cutting for later use.

2.6. Fabrication of the micro-structured conductive layer

Fabrication of the micro-structured conductive layer is shown in Fig. S2d (online). First, a customized wax mold with inversed pyramid structures (length and height are both 1 mm) was subjected to plasma surface treatment for about 20 min to obtain clean surface. Secondly, ES-PU solution (29 wt%) was poured into the wax mold and placed at room temperature for 2 d until the precursor solution completely dried into a solid film. The film was peeled off from the wax mold and cut into specific shape by laser cutting. Thirdly, the pyramid structured side of the film was coated with a thin layer of conductive Ag ink via a sponge and dried in oven at 65 °C about 30 min, resulting a microstructured conductive layer.
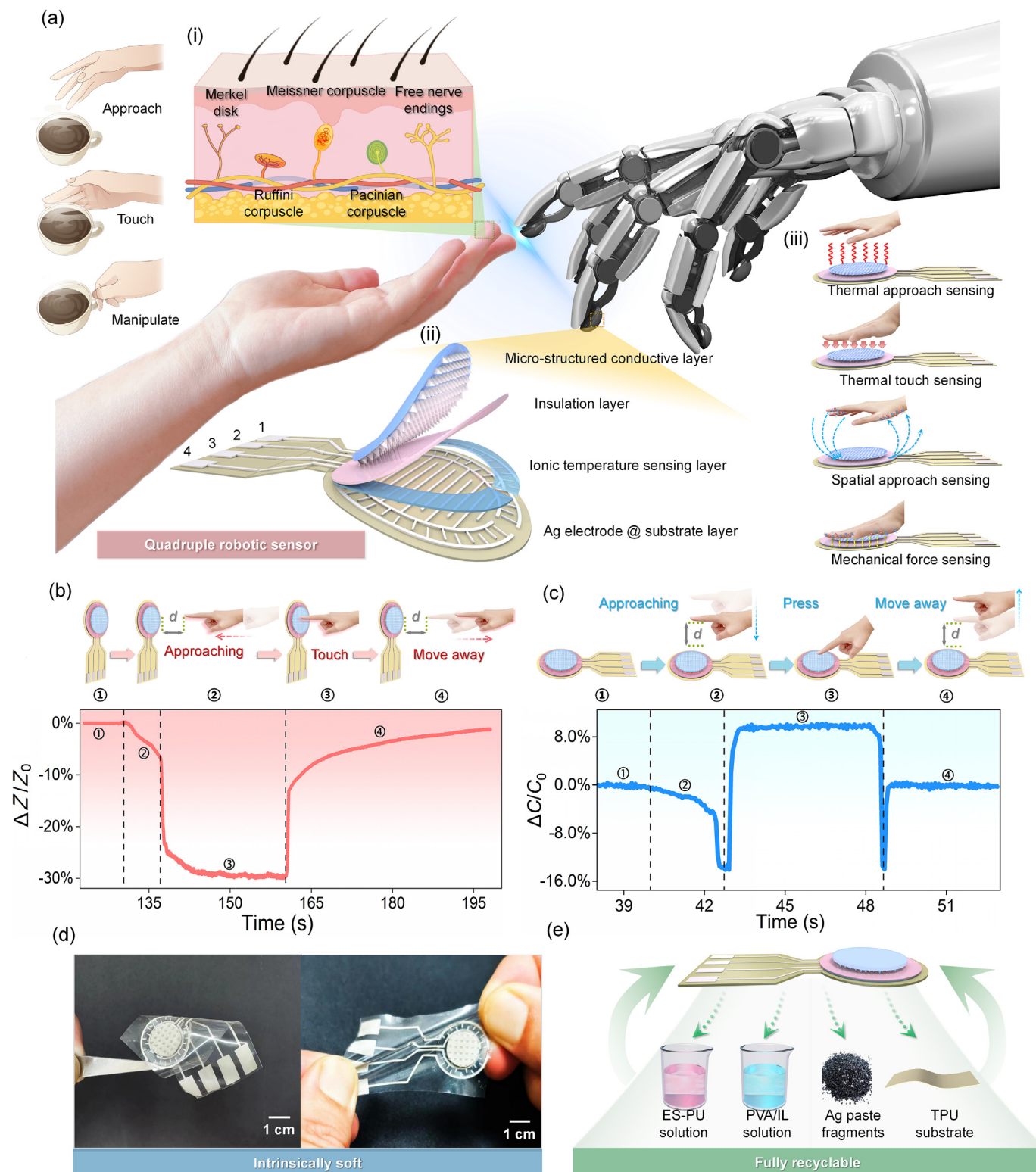
Fig. 1. Design concept and typical response of the robotic sensors. (a) Design concept and configuration of the robotic sensors with quadruple sensing functions for reliable HRI. (i) Schematic diagram showing the sensing capabilities of natural skin with diverse sensory receptors for object perception and manipulation. (ii) Composition and structure layout of the robotic sensors. (iii) Quadruple sensing functionalities of the robotic sensors, including thermal approach sensing, thermal touch sensing, spatial approach sensing, and mechanical force sensing. (b) Schematic diagrams showing the consecutive thermal approach and thermal touch sensing processes and the typical response behaviors. (c) Schematic diagrams showing the consecutive spatial approach and mechanical force sensing processes and the typical response behaviors. (d) Digital pictures showing the flexibility and softness of the fabricated robotic sensors. (e) Schematic illustrating the recyclability of the robotic sensors.

2.7. Assemble and fabrication of the robotic sensors

Assemble and fabrication of the robotic sensors are shown in Fig. S3 (online). At first, the TPU substrate with printed Ag electrode patterns was cut into specific shape and size. Then, two PVA/IL layers were pasted on the temperature sensing area of the Ag electrodes using the original PVA/IL solution. Secondly, the ES-PU insulation layer was pasted on the top surface of the sensors to encapsulate the temperature sensing layer with ethanol. Thirdly, the micro-structured conductive layer was pasted on the top of the insulating layer at the central sensing region with ethanol. Finally, the assembled robotic sensors were placed in an oven at 65 °C for 30 min to totally remove the solvents. For sensing performance characterizations, the sensor size was 5 cm in length and 2.8 cm in width. For integration with the robotic grippers, the sensor size was set to be 2.5 cm in length and 1.4 cm in width to accommodate the gripper finger size.

2.8. Construction of the sensor-integrated robotic system

The prepared robotic sensors were affixed to the surface of the soft grippers (F-B4T/LS1, China) with double-sided tapes. The sensors were also connected to the test port of the data collection module (JYE Tech, M162LCR, China). The sensor data were transmitted in real-time to the master module (LOCKZHINER Electronic, STM32H750) through the serial port J5 on the data collection module. After signal processing by the master module, specific instructions were issued to the DAC (LOCKZHINER Electronic, DAC8563) according to the predefined program to regulate the air pressure and control the soft grippers. Digital signals were converted into 0–10 V analog signals for controlling the electric valve (SMC, ITV1050-312l, Japan).

A high-pressure air of 0.8 MPa was supplied by an air compressor (XIYE tech, XYYS100, China). The compressed air passed through an air filter and a pressure-reducing valve (AIRTAC, GAL300-08, China) to reduce the air pressure. Following the air filter and pressure-reducing valve, a proportional valve was used to arbitrarily control the air pressure in real-time, thus to control the grasping movement of the soft gripper.

2.9. Control of the robotic arm

Based on the robot system and QT software, an interactive control program is developed to control the robot system. The six-degree-of-freedom robotic arm can be controlled via a PC terminal by establishing communication with the robot controller using the RS485 protocol.

2.10. Application of the robotic sensors for HRI

The developed robotic sensors were integrated into the gripper fingers for object manipulation monitoring and onto the gripper base for collision warning with human body. The sensor signals for object manipulation monitoring and collision warning were collected with a high-speed LCR meter. For object recognition scenario, we selected 20 objects with varying shapes and sizes. The grasping process was initiated by issuing commands from the master module, which controlled the DAC to increase the voltage output to the proportional valve, thereby driving the soft gripper to grasp these objects.

For non-contact thermal approach sensing scenario, we employed six cups of water with temperatures of −40 °C (using dry ice), 0 °C (using ice-water mixture), 25 °C (room temperature water), 50 °C (warm water), 75 °C (hot water), and 100 °C (boiling water), respectively. The robotic arm was controlled with a PC and directed to descend at a rate of 50 mm/s to approach the water cups gradually, finally stopping at a distance of 1 cm. At this point, the data collection module collected the impedance signal from the sensors. The signal was then transmitted to the master module for date processing. If the sensor signal exceeded the predefined safety threshold, indicating a hazardous temperature, the soft gripper was not deployed for grasping. At the same time, the master module sent the temperature recognition results to the PC terminal and display the results on the PC software interface. On the contrary, if the target temperature was at a safe level, the soft gripper was deployed to grasp the water cups. The soft gripper sequentially grasped the water cups to detect the water temperature in a contact manner. After detecting the precise temperature of the objects, the robotic arm would pick up the water cup with the right temperature, and give it to the patient.

2.11. CNN mode for object recognition

A Convolutional Neural Network (CNN) was trained to recognize the grasped objects. For the 20 objects, a total of 20×50 sets of data were collected. Each dataset is a 2D image of the response signal collected during grasping a specific object. A python script was programmed to generate 2D plots in batches from the real-time exported Excel data and to proceed data normalization simultaneously. The original signal plots were normalized to achieve more reliable recognition. The CNN model consists of three convolution layers, three max pooling layers and two fully-connected layers. The first, second, and third convolution layers have 8, 16, and 32 channels respectively. The size of the convolution kernels is 3×3 and the activation function is Rectified Linear Unit (ReLU) function. For the kernels of the max pooling layers, the size is 2×2. The first fully connected layer consists of 128 neurons with the ReLU function as the activation function. The subsequent fully connected layer comprises 20 neurons, employing the Softmax function as the activation function for classification. As for dataset division, 70% dataset (700 plots) were used as training set, 10% dataset (100 plots) were used as a cross-validation set for model validation and the residual 20% dataset (200 plots) were used as test set for model iteration and optimization. The initial learning rate was set as 0.001 and 100 epochs have been trained in this process.

2.12. Recycling process of the robotic sensors

The recycling process of the robotic sensors is described as follows. At first, the top micro-structured conductive layer (consisting of ES-PU and silver paste) and the insulation layer (consisting of ES-PU) were peeled off from the sensors and immersed into ethanol for dissolution. After 1.5 h stirring, the ES-PU material can be completely dissolved by ethanol, resulting in ES-PU ethanol solution with silver paste fragments. The silver paste fragments could be easily filtered and dried for reuse. The ES-PU ethanol solution could also be dried into ES-PU film again.

Secondly, the ion temperature sensing layer (consisting of PVA/IL) was peeled off from the sensors and immersed into deionized water. Due to the water-soluble characterization of PVA and IL, an aqueous solution of PVA/IL could be obtained after mechanical stirring. PVA/IL film could be regenerated by drying the PVA/IL aqueous solution again.

Thirdly, the remaining layer of Ag interdigital electrode printed on TPU substrate was put into ethanol-acetone mixture (80% / 20% in weight ratio) to swell the TPU substrate. After heating, stirring and 30 min ultrasonic treatment, the printed Ag electrode would detach from the TPU substrate due to the swelling of the TPU substrate. The final TPU substrate was dried for reuse. The detached silver paste fragments could be easily filtered and dried for reuse.

2.13. Characterization and measurement

The scanning electron microscopy (SEM) images were conducted using a scanning electron microscope (Hitachi Regulus 8220, Japan). Digital pictures were recorded by professional camera (Panasonic DC-S5M2, Japan). Optical microscope pictures were photographed by high-definition electron microscope (Zongyuan ZY-H5000, China). Heating and stirring in the fabrication process was conducted by magnetic stirrers (JOANLAB HS-17, China). The laser cutting process was conducted by laser engraving machine (FST Laser FST-3020, China). The drying process was conducted in an air-drying oven (Bluepard DHG-9035A, China). The ultrasonic treatment process was conducted by ultrasonic cleaner (Kemeng KM-36C, China). Mechanical sensing performance was calibrated using a digital force gauge (Handpi Instruments HLD, China). The capacitance and impedance signals of the sensors were collected on a high-speed LCR meter (Tonghui TH2817B, China) at the frequency of 10 kHz. FTIR was conducted on an infrared spectrometer (Nicolet iS50, America) to study the chemical structure of ES-PU film. The molecular weight of ES-PU was measured by a gel permeation chromatography (GPC, HLC-8320) with DMF as eluent and polystyrene as standard. The tensile properties were performed at room temperature on a universal testing machine (QLW-5E, Xiamen Qunlong Instrument Co., LTD, China). ^{1}H NMR was performed on NMR spectrometer (JNM-ECZ400S/L1) at 400 MHz with the CDCl$_3$ as solvent to confirm the structure of ES-PU.

3. Results and Discussion

3.1. Design concept and principle

Natural skin is equipped with diverse types of receptors to gather comprehensive information (Fig. 1a-i) and to safely and efficiently interact with the physical world. Taking the scenario of manipulating a cup of hot coffee as an example (Fig. 1a-i), the coffee temperature can be firstly perceived by approaching the cup gradually, to safely estimate the rough temperature to avoid empyrosis. The specific temperature, texture and weight can be further evaluated by touching the cup. Then, the coffee cup could be picked up and handled dexterously for drinking. During this whole process, the brain utilizes abundant tactile information to coordinate the muscles, ensuring these actions are performed accurately and safely.

To endow robotic systems with similar sensing capabilities as found in nature skin, we propose a novel type of soft robotic sensors with quadruple sensing functionalities via rational material engineering and spatial configuration design (Fig. 1a-ii). The quadruple sensing functions include thermal approach sensing, spatial approach sensing, thermal touch sensing, and mechanical force sensing (Fig. 1a-iii). The thermal approach sensing function is realized based on thermal radiation effect, while the thermal touch sensing function depends mainly on thermal conduction effect. The spatial approach sensing function utilizes electric field coupling effect between external object and the robotic sensors, while the mechanical force sensing function is based on mechanical regulation of capacitor parameters. The detailed four sensing mechanisms are fully elaborated below.

Typical response behaviors of the robotic sensors are shown in Fig. 1b and c. Specifically, thermal approach sensing process gives rise to slow variation of the ionic impedance signal (Fig. 1b②) measured between the electrode 1&2 and electrode 3&4, while thermal touch sensing process leads to dramatic change in the ionic impedance signal (Fig. 1b③). Spatially approaching the sensors with an object causes a gradual decline in the capacitance signal (Fig. 1c②) measured between electrodes 2 and 3, while

applying a mechanical force upon the sensors results in dramatic increase in the capacitance signal (Fig. 1c③). Once the external object is removed from the sensors, both of the two types of signals could fully recover to the initial levels.

Another advantage of the robotic sensors is the remarkable softness, as all of the sensor components comprise intrinsically soft and elastic materials. The fabricated robotic sensors can be easily bent or even stretched (Fig. 1d), which endows the sensors with good conformability to 3D curved surfaces. Additionally, all of the sensor ingredients could be fully recycled and reused upon the sensor's end of service (Fig. 1e, discussed below), possessing good cost effectiveness and environmental friendliness.
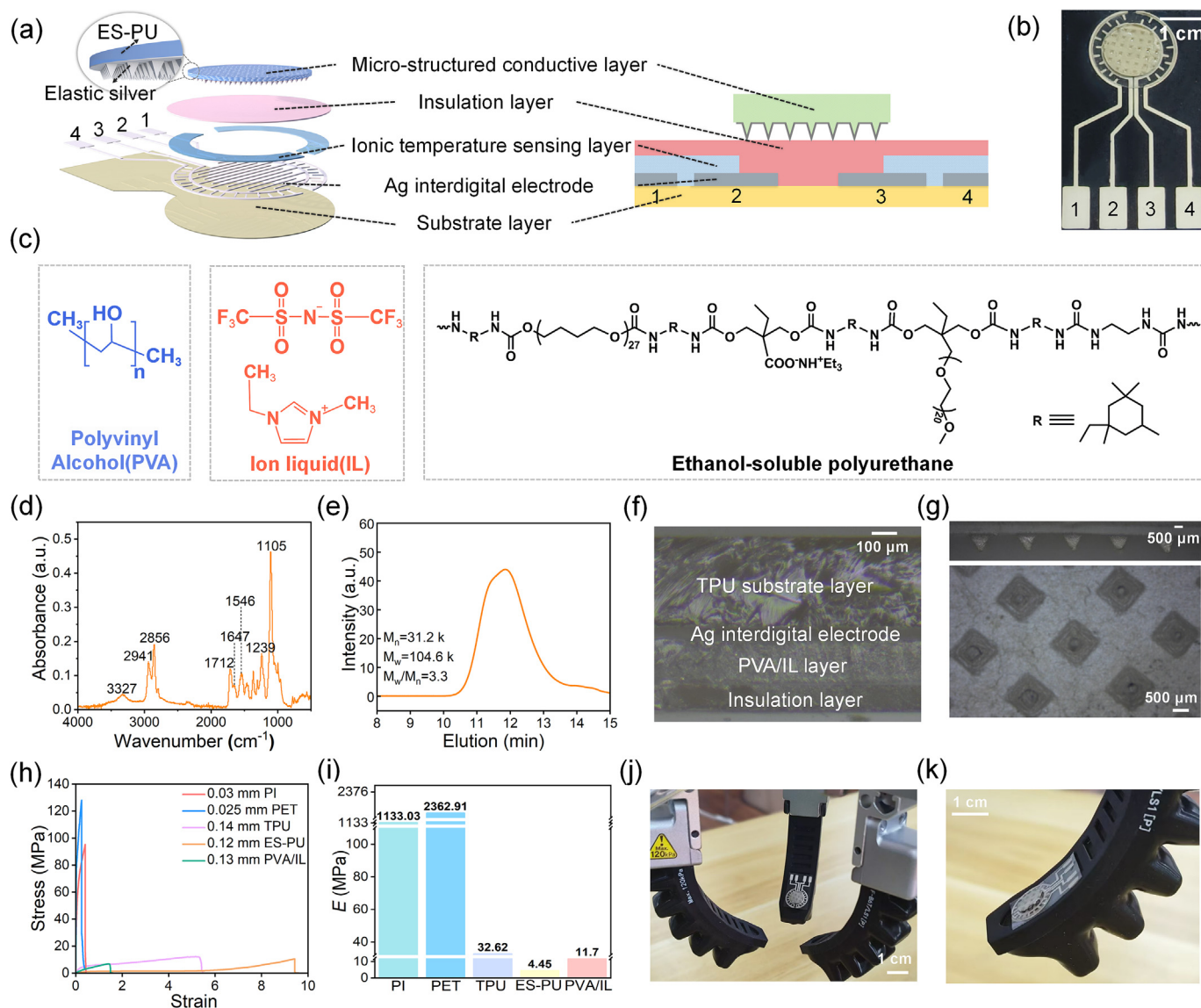
3.2. Fabrication and characterization

The structure layout and sectional view of the robotic sensors are presented in Fig. 2a. The sensors comprise five layers totally, including a soft substrate layer, four silver (Ag) interdigital conductive electrodes, two ionic temperature sensing layers, a soft insulation layer, and a top micro-structured conductive layer. A digital picture of the fabricated sensors is shown in Fig. 2b.

Thermoplastic polyurethane (TPU) is used as the soft substrate layer, onto which elastic Ag interdigital electrodes with self-defined patterns are printed. The ionic temperature sensing layers with ionic conductivity are composed of polyvinyl alcohol (PVA) and ionic liquid (IL, [EMIM]$^+$[TFSI]$^-$) (Fig. 2c). The soft insulation layer is made from a self-designed and self-synthesized ethanol-soluble polyurethane (ES-PU) material. The synthetic method and molecular structure of the ES-PU is given in Fig. S1 (online) and Fig. 2c. The top micro-structured conductive layer is constructed by casting a micro-structured ES-PU film first, followed by printing elastic Ag paste onto the micro-structured surface. Detailed fabrication processes of the individual layers and the final assembly process of the sensors are elaborated in the Experimental Section and Figs. S2 and S3 (online).

The synthesized ES-PU material is first characterized with Fourier transform infrared spectroscopy (FTIR). As shown in Fig. 2d, the characteristic peaks at 3327 and 1546 cm^{-1} are attributed to the N–H stretching vibrations of urea and urethane groups. The peaks at 2941 and 2856 cm^{-1} correspond to the C–H stretching vibrations. The C=O stretching vibration from urethane and urea groups can be clearly observed at 1712 and 1647 cm^{-1}, respectively. The peak at 1239 cm^{-1} is assigned to the C–O–C asymmetric stretching vibration from the urethane group, and the 1105 cm^{-1} ascribes to the C–O–C symmetric stretching vibration from PTMG and Ymer N120. The characteristic peak at 2265 cm^{-1} belonging to the isocyanate group disappears completely. All characteristic peaks correspond to the designed ES-PU structure in Fig. 2d. Moreover, the synthesized ES-PU exhibits a number average molecular weight (Mn) of 31.2 k with a polydispersity index of 3.3 based on Gel Permeation Chromatography (GPC) characterization (Fig. 2e). These results indicate that the designed ES-PU has been successfully synthesized and the relative molecular weight is estimated to be 105.2 k (Fig. 2e).

The cross-sectional morphology of the sensors with a multi-layered structure is observed with optical microscope (Fig. 2f). From the microscope image, the TPU substrate layer, the Ag interdigital electrode, the PVA/IL temperature sensing layer, and the ES-PU insulation layer could be clearly recognized. The periodic pyramid structure of the top micro-structured conductive layer is presented in Fig. 2g.

The mechanical properties of the main components (i.e., TPU layer, ES-PU layer, and PVA/IL layer) of the sensors are also investigated. The most commonly used flexible substrates (e.g., polyethylene terephthalate (PET) and polyimide (PI)) are employed for

Fig. 2. Fabrication and characterization of the robotic sensors. (a) Schematic diagram showing the three-dimensional structure layout and two-dimensional sectional view of the robotic sensors. (b) Photograph of the robotic sensors. (c) Molecular composition and structure of the essential components (i.e., PVA, IL, and ES-PU) in the robotic sensors. (d, e) FTIR spectroscopy and GPC spectrum of the self-synthesized ES-PU materials. (f) Optical microscopy image showing the cross-section morphologies of the robotic sensors. (g) Optical microscopy images showing the engineered pyramid patterns on the top micro-structured conductive layer. (h, i) Stress–strain curves and Young's modulus of the TPU layer, ES-PU layer, and PVA/IL layer. Conventional PET and PI films are used for comparison. (j, k) Digital pictures showing soft robotic sensors conformed with 3D curved and dynamically-changing soft grippers.

comparison. As shown in Fig. 2h and i, the TPU layer, ES-PU layer, and PVA/IL layer in our sensors exhibit much higher stretchability (531%, 943%, and 146%) and lower Young's modulus (32.6, 4.5, and 11.7 MPa) than that of conventional PET and PI materials. Therefore, the fabricated robotic sensors have good intrinsic softness and can be seamlessly conformed with 3D curved or dynamically-changing surfaces, e.g., soft robotic grippers (Fig. 2j, k).

3.3. Sensing mechanisms and performance

The quadruple sensing functions and the related responsive behaviors of the robotic sensors are presented in Fig. 3. Both of the thermal approach sensing and thermal touch sensing are realized by measuring the ionic impedance (Z) between the electrode 1&2 and electrode 3&4, as shown in Fig. 3a and Fig. 3e. The impedance of the temperature sensing layers is highly dependent on

external temperature (T) variations based on the following equation:

$$Z \sim Z_0 e^{\frac{0.12E(T_0-T)}{TT_0}},\qquad(1)$$

where Z_0 is the initial impedance value, T_0 is the initial temperature, E denotes activation energy [33]. The key difference between thermal approach sensing and thermal touch sensing lies in the heat transfer mechanisms: the former depends on thermal radiation effect in a non-contact manner (Fig. 3a), while the latter relies on thermal conduction effect through contact (Fig. 3e). Thermal radiation effect can be described with the Kirchhoff's law:

$$T \sim Q = \frac{K\Delta TS}{d^2},\qquad(2)$$

where Q is the amount of heat radiated from the heat source, K represents thermal radiation constant, ΔT stands for temperature dif-
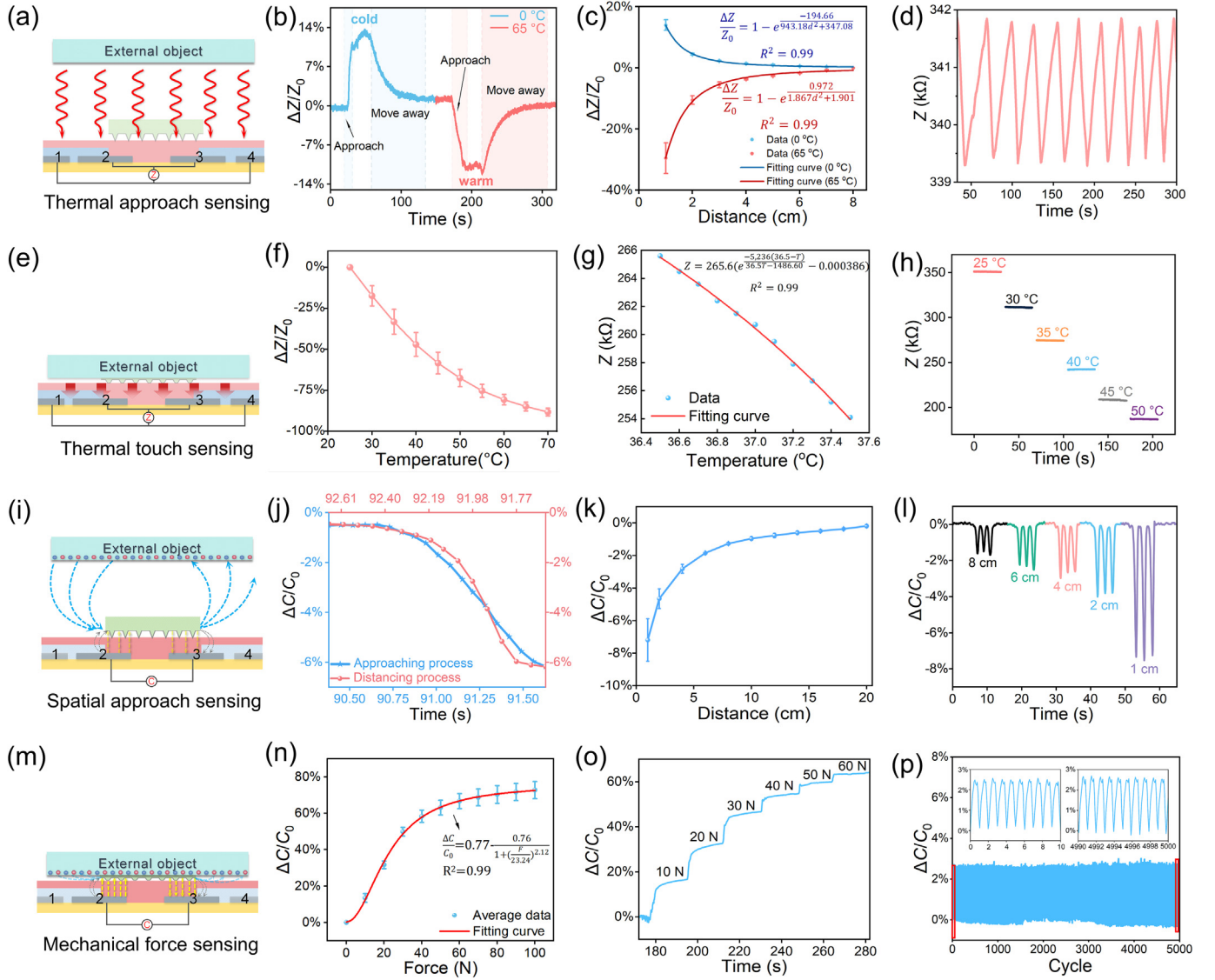
Fig. 3. Sensing mechanisms and performance characterizations of the robotic sensors. (a) Schematic illustrating the thermal approach sensing mechanism based on thermal radiation effect. (b, c) Response behaviors and calibration curves of the sensors to a cold object (0 °C) approaching and a hot object (65 °C) approaching. (d) Response behaviors of the sensors to repeated approaching and removing of a warm hand from far away to 1 cm from the sensors. (e) Schematic illustrating the thermal touch sensing mechanism based on thermal conduction effect. (f) Calibration curves of the sensors when contacting with objects of different temperatures. (g) Minimum temperature detection resolution of the sensors in thermal touch sensing. (h) Response signals of the sensors to different stable environment temperatures. (i) Schematic illustrating the spatial approach sensing mechanism based on electric field coupling effect. (j) Response behaviors of the sensors when a hand approaches the sensors gradually and then moves away. (k) Calibration curve of the sensors for spatial approach sensing. (l) Signal variations of the sensors when a hand repeatedly approaches the sensors at different distances. (m) Schematic illustrating the mechanical force sensing mechanism based on modulation of capacitor parameter. (n) Calibration curve of the sensors for mechanical force sensing. (o) Response behaviors of the sensors to stable mechanical forces of different magnitudes. (p) Repeatability and reliability of the sensors during 5000 cycles of loading–unloading test.

ference between heat source and sensors, S denotes the intersection area, and d indicates the distance between heat source and sensors. In comparison, thermal conduction effect can be described with Fourier's law:

$$T \sim Q = K\frac{\mathrm{d}T}{\mathrm{d}y}S, \tag{3}$$

where Q is the amount of heat conducted from the heat source, K presents thermal conductivity, $\frac{\mathrm{d}T}{\mathrm{d}y}$ means the temperature gradient between heat source and sensors in the direction of contact and S indicates the contact area of heat-transferring objects. Based on the above equations, thermal approach sensing mainly relies on the distance and temperature difference, while thermal touch sensing mainly depends on the temperature gradient and contact area.

The thermal approach sensing behaviors (measured at 25 °C) are shown in Fig. 3b–d. When a cold (0 °C) or hot (65 °C) object approaches to the sensor gradually, the measured impedance signal exhibits a corresponding increase (or decrease) and can fully recover to its initial value after removal of the object (Fig. 3b). The maximum signal variations are closely related to the distance (d) between the object and the sensors (Fig. 3c). Mathematical fitting is performed on the experimental data (see the Note S1 online for the detailed fitting process) and the fitting results are shown in Fig. 3c. The correlation coefficient between the fitting curve and experimental data is 0.99. Thus, the approaching distance of an object with specific temperature can be quantitatively evaluated. Notably, the approaching detection range can reach up to 8 cm. Fig. 3d shows the signal variations when a warm human hand

repeatedly approaches to the sensors, revealing desirable repeatability and reproducibility of the thermal approach sensing function. The effects of environmental temperature and size of the objects on the sensor response are also investigated, which are presented in Figs. S4 and S5 (online).

The thermal touch sensing behaviors are shown in Fig. 3f–h. When the sensor contacts with objects of different temperatures, the sensor signal variations show significant differences (Fig. 3f), allowing us to quantitatively calibrate the sensors. The minimum temperature detection limit can be down to 0.1 °C (Fig. 3g), revealing high sensitivity and resolution of our sensors. The correlation coefficient between the fitting curve of Fig. 3g and the experimental data is 0.99. Additionally, the sensor signals remain highly stable under different environment temperatures (Fig. 3h), demonstrating the sensor's capability to continuously monitor static or varying thermal stimulations. The thermal touch sensing repeatability is also verified, as given in Fig. S6 (online).

The spatial approach sensing and mechanical force sensing are realized by measuring the capacitance (C) between the electrodes 2 and 3, as shown in Fig. 3i and Fig. 3m. The main difference between these two functionalities lies in the capacitance regulation mechanisms: the former depends on electric field coupling effect between the sensor and the external objects (Fig. 3i), while the latter relies on capacitor parameter (i.e., electrode spacing) modulation (Fig. 3m).

The spatial approach sensing mechanism is illustrated in Fig. 3i. The sensor itself can be regarded as a capacitor with a self-capacitance (C_s). When a conductive object (i.e., human hand, metal plate, etc.) approaches to the sensors, the fringing field of the sensors can be affected (Fig. S7a online). The capacitance coupling between the object and the sensors gives rise to a mutual capacitance (C_m). The capacitance of the whole system (C_0) can be regarded as a stable value since the approaching of external object would not alter the system parameters. Thus, the influence of external object approaching on the self-capacitance (C_s) signal of the sensors can be described with the following equation:

$$C_s \sim C_0 - C_m = C_0 - \frac{4\varepsilon w_{mc}}{\pi} \ln \frac{2l_{mc}}{d_{mc}}, \tag{4}$$

where ε represents the relative permittivity, w_{mc} and l_{mc} represent the width and length of the target object, d_{mc} represents the distance between the electrode and the target object. Based on this mutual coupling effect, the spatial approaching of a targeted object can be detected.

As shown in Fig. 3j and Fig. S8 (online), when a human hand approaches the sensors gradually and then moves away, the recorded signal decreases first and then shows a reversible recovery. The relationship between the approaching distance and the capacitance signal is presented in Fig. 3k. A detection range up to 20 cm can be achieved. Fig. 3l shows the response behaviors when a hand repeatedly approaches the sensors at different distances, indicating the capability of the sensors in detection of object approach distance. The signal stability could be further improved by optimizing the test environment (Fig. S9 online). In addition, the influence of different environmental factors on the spatial approach sensing performance of the sensors is explored. The results demonstrate that the sensors are susceptible to electromagnetic interference, but not sensitive mechanical vibration and humidity variation (Fig. S10 online).

When an external object contacts and then applies a mechanical force upon the sensors, the capacitor parameter of the sensors (i.e., electrode spacing) can be regulated. Specifically, when measuring the capacitance between the electrode 2 and 3, the sensors can be regarded as two capacitors connected in series (Fig. S7b online).

One capacitor is formed between electrode 2 and the top micro-structured electrode, while the other capacitor is formed between electrode 3 and the top micro-structured electrode. With the micro-structured electrode design, the electrode spacing in these two capacitors can be modulated by external force, as the pyramid structure on the top electrode is mechanically deformable. Therefore, applying a mechanical force on the sensors will decrease the electrode spacing and increase the measured capacitance signal between electrode 2 and 3 (Fig. 3m) based on the equation of $C=\frac{\varepsilon S}{d}$, where ε denotes the relative permittivity, S and d indicate the overlap area and distance between the electrodes, respectively. The typical response behaviors of the sensors when pressed by a finger are shown in Figs. S11 and S12 (online), from which the spatial approach and mechanical press processes can well reflected. Fig. 3n exhibits the calibration curve of the mechanical force sensing process. A fitting equation is also provided, with the correlation coefficient and error offset calculated to be 0.99 and 10.9%, respectively. Additionally, the capacitance signal remains stable under a specific force (Fig. 3o), revealing the capability to continuously monitor and distinguish external force. The signal response during loading and unloading a cyclic force for 5000 times is given in Fig. 3p. The baseline drifting and peak point drifting are calculated less than 0.36% and 0.48% respectively.

Finally, the mutual interference between different sensing mechanisms is investigated. The results show that the robotic sensors are able to decouple thermal stimuli and mechanical stimuli (Fig. S13 online). This is because these two types of stimuli are detected based on different parameter measurements.

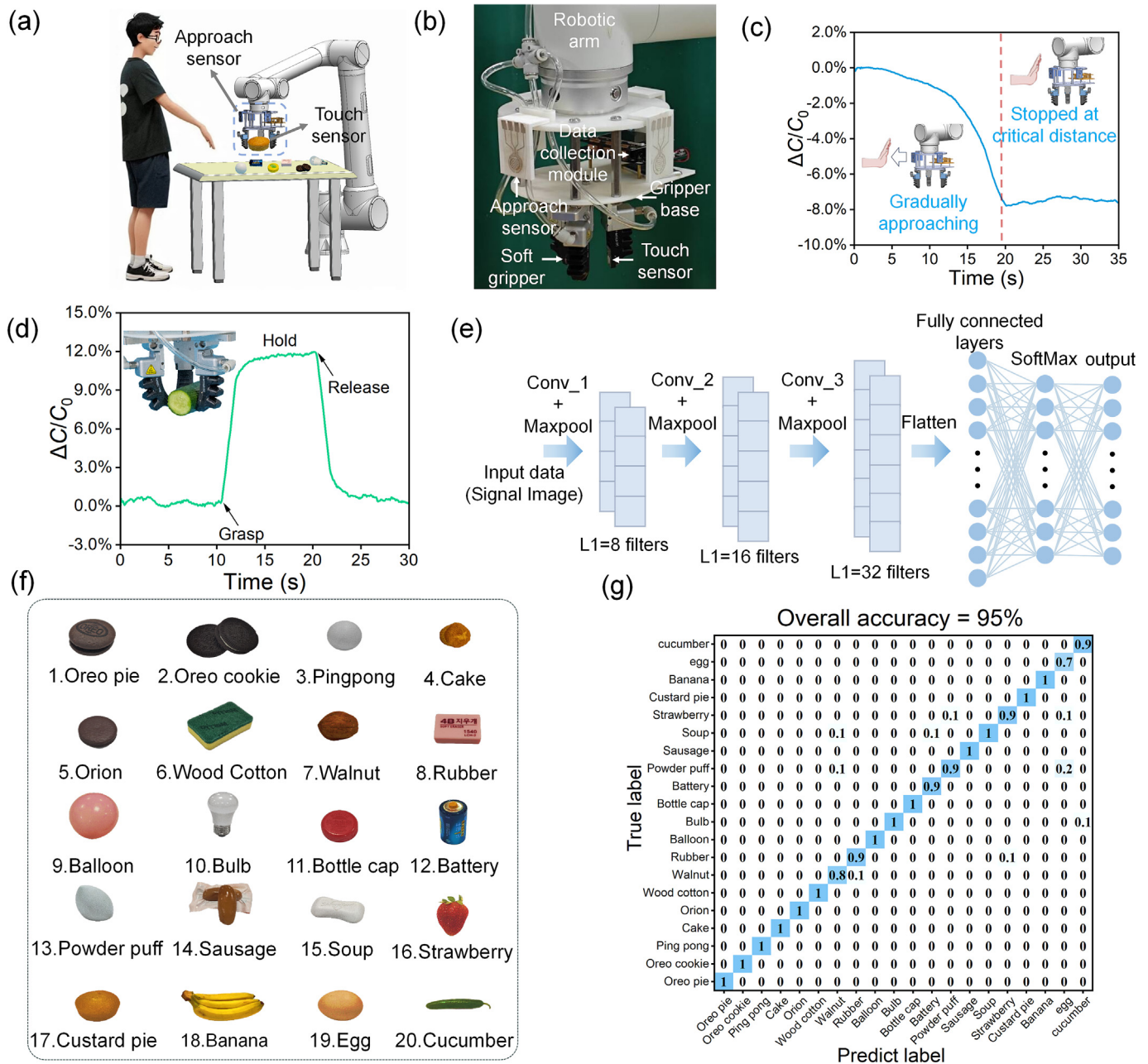### 3.4. Application of robotic sensors in HRI

Robotic sensors play a vital role for safe and efficient HRI, especially in unstructured or dynamic environments. Compared with the developed sensors with single or two functions, our proposed robotic sensors integrate quadruple sensing functionalities and offer a more versatile solution for HRI applications. As demonstrations, a programmable robot arm system with a pneumatic soft gripper integrated as the robot end effector is employed (Fig. 4a). The proposed robotic sensors are installed onto the gripper fingers and the gripper base, respectively (Fig. 4b). The sensor-integrated robotic gripper and arm system is shown in Fig. 4b. The sensor integration on the gripper fingers is for object manipulation monitoring, while the sensor installation on the gripper base is for dangerous collision warning with human body.

Firstly, we investigate the collision warning scenario with human body. As shown in Fig. 4c, when the robot end effector is approaching the human body gradually, the recorded capacitance signal of the sensors shows a continuous decline based on the spatial approach sensing function. A critical warning distance (e.g., 1 cm) can be set to avoid the dangerous collision. Once the distance between the robot and the human body goes down below 1 cm, the movement of the robot arm could be stopped to guarantee the HRI safety.

The robotic sensors installed on the gripper fingers could be used to resolve the grasping force during object manipulations. Fig. 4d presents a typical response signal of the sensors when grasping, holding, and releasing an object (e.g., cucumber). Based on the characteristics of the sensor signal during object grasping, the object properties could be reflected. The response signals are closely related to the hardness of the objects (Fig. S14 online). In addition, other object properties (e.g., size, shape, deforming behavior, and so on) could be reflected in the signal features (e.g., slope, shape, duration, etc.).

To further investigate the feasibility of recognizing and classifying more different objects, a convolutional neural network
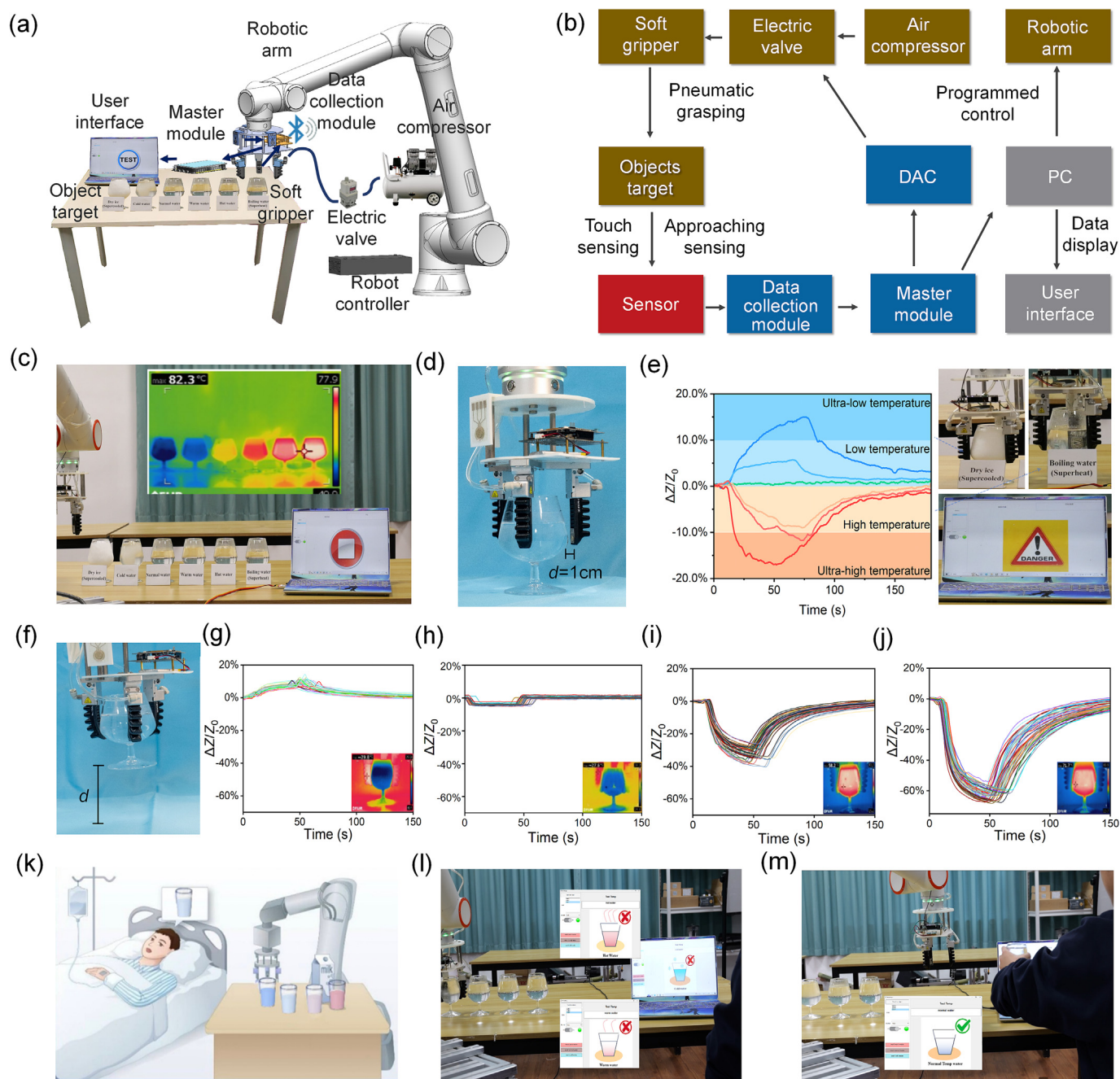
Fig. 4. Applications of the robotic sensors for collision warning with human body and AI-assisted object recognition. (a) Schematic showing a programmable robot arm system integrated with the robotic sensors for HRI. (b) Digital picture showing the robotic sensors integrated on gripper fingers (for object manipulation monitoring) and gripper base (for dangerous collision warning). (c) Response signal of the robotic sensors when a human hand gradually approaches the robot arm and then stops at a critical distance of 1 cm. (d) Response behaviors of the sensors when the soft gripper grasps, holds, and releases a cucumber. (e) Structure diagram of the convolutional neural network (CNN) model used for object recognition. (f) Digital pictures of 20 different daily objects employed for the test. (g) Confusion matrix showing the recognition accuracy of the 20 objects.

(CNN) model is employed to analyze the response signal features when grasping different objects. The structure of the CNN model is presented Fig. 4e, which consists of three convolutional layers, three max pooling layers, a fully connected layer, and a SoftMax classifier. We totally employ 20 kinds of various objects in daily life with different size, shape, and material properties to evaluate the object recognition reliability (Fig. 4f). The typical response signals corresponding to each object grasping are presented in Fig. S15 (online), while the collective signals during grasping six representative objects for 50 time are shown in Fig. S16 (online). These original sensor signals are converted into two-dimensional images for the train-

ing and testing of the CNN model. 50 images are collected for each object, and the database containing 1000 images is totally involved. The confusion matrix shows that an overall accuracy of 95% can be achieved for the recognition and classification of the 20 daily objects (Fig. 4g). In addition, by de-noising the pristine sensor signals, the recognition rate could be further improved to 98% (Fig. S17 online).

In addition to spatial distance and mechanical force detection, we further demonstrate the thermal approach sensing and thermal touch sensing functions of the robotic sensors using a self-built close-loop-controlled robot system. The system composition and control principle are presented in Fig. 5a and b, respectively. The

Fig. 5. Applications of the robotic sensors for thermal approach sensing, thermal touch sensing and feedback control of the HRI system. (a, b) Schematic illustration and block diagram showing the main components and operating principle of the close-loop controlled robotic system, including functions of sensor data collection and transmission, sensor date processing and visualization, close-loop control of the robotic arm movement, and close-loop control of the pneumatic gripper. (c) Optical and infrared images of six cups of water with different temperatures (−40, 0, 25, 50, 75, 100 °C). (d) Photograph showing that the soft gripper approaches the objects with a minimum distance of 1 cm for thermal approach sensing. (e) Response signals of the sensors during approaching six cups of water of different temperatures. The objects with defined dangerous temperatures (−40 °C in dark blue region and 100 °C in dark orange region) can be recognized and the soft gripper would not grasp these dangerous objects in the following process. (f) Photograph showing the soft gripper grasps the target objects. (g–j) Sensor response signals when repeatedly grasping the selected four objects with safe temperatures (0, 25, 50, and 75 °C) for 50 times. (k) Schematic showing the potential application scenario of the robot system for bedside clinical care. (l, m) Photographs showing the robot system equipped with our sensors for recognizing and taking the water of right temperature (e.g., 25 °C) for the patient from the four cups of water of different temperatures.

digital picture of the entire system is shown in Fig. S18 (online). The whole system is controlled by a master module, including functions of original sensor data collection and transmission, sensor date processing and visualization on a PC interface, close-loop control of the robotic arm movement, and close-loop control of the pneumatic gripper. All of the details are elaborated in the experimental section.

The system is designed to utilize the non-contact thermal approach sensing function to exclude objects with extremely low or high temperature, thus to avoid the possible damage to the soft pneumatic gripper during direct contact with these objects (Fig. 5c–e). Then, objects with safe temperature are manipulated and evaluated based on thermal touch sensing function in contact manner (Fig. 5f–m).

As shown in Fig. 5c, six cups of water of different temperatures (−40, 0, 25, 50, 75, 100 °C) are used as the targeted objects, where −40 and 100 °C are defined as the dangerous temperature. Then, the soft gripper is commanded to approach the six cups of water and stop at a minimum distance of 1 cm (Fig. 5d). In this manner, the object temperature can be evaluated in a non-contact sensing style with desirable reliability (Fig. S19 online). The response signals of the sensors during approaching the six cups of water are presented in Fig. 5e. By setting the warning regions (e.g., dark blue or dark orange), the objects with dangerous temperatures can be recognized (Fig. 5e right, and Movie S1 online) and the soft gripper would not grasp these dangerous objects in the following process.

Based on the above procedure, the four cups of water with safe temperatures (0, 20, 50, and 75 °C) are screened out. Subsequently, the specific temperatures of the four cups of water are further evaluated in a contact manner. The soft gripper is further pressurized to directly contact and grasp the target objects (Fig. 5f), and the response signals of the sensors are shown in Fig. 5g–j. It can be observed that, during 50 times of repeatedly grasping, the response curves of the sensors exhibit high similarity with each other, indicating high reliability of this contact sensing process.

This above-presented robot system with real-time sensation and close-loop controlled actuation can find promising applications in bedside clinical care. For example, it is difficult for an incapacitated patient to get the wanted items, e.g., a cup of water with specific temperature (Fig. 5k). So, the robot system could help to perceive the temperature of the water cups sequentially, and pick up the water cup of right temperature for the patient, as demonstrated in Fig. 5l, m and Movie S2 (online).

In addition to spatial approach and mechanical force sensing, as well as thermal approach and touch sensing, we further explore some hybrid sensing scenarios. For example, when combining spatial approach sensing and thermal approach sensing, the same object with different temperatures or different objects of the same temperature can be well distinguished (Fig. S20 online). Also, when combining mechanical force sensing and thermal touch sensing, both the object's temperature and softness can be recognized (Fig. S21 online). Finally, spatial approach sensing, mechanical force sensing, thermal approach sensing, as well as thermal touch sensing could be fully combined to perform more complex object recognitions (Fig. S22 online). Overall, rational combinations of the quadruple sensing functions create many possibilities for HRI systems.
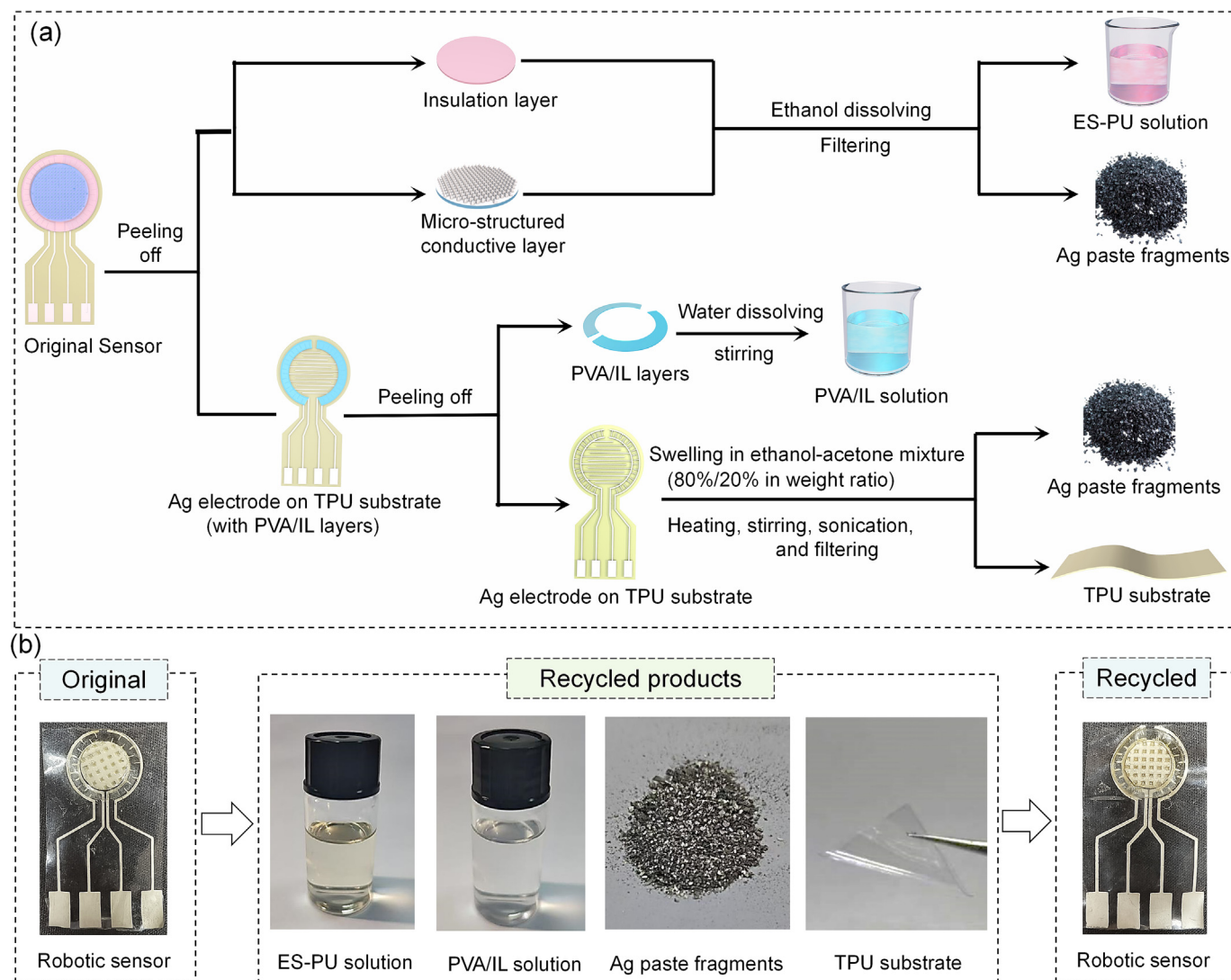
Fig. 6. Recycling process of the robotic sensors. (a) Schematic illustrating the full recycling process of the robotic sensors based on an eco-friendly method. (b) Digital pictures showing the recycled products from the sensors, including ES-PU ethanol solution, PVA/IL aqueous solution, Ag paste fragments, and TPU substrate. These recycled products can be reused to reconstruct new batch of robotic sensors.

3.5. Recyclability of the robotic sensors

Some components (e.g., silver and ionic liquid) in the robotic sensors are expensive. Reuse of these materials can reduce the manufacturing cost. Also, the robotic sensors integrated on robotic grippers would inevitably suffer abrasion and damage. Regular replacement of the sensors is necessary. Therefore, endowing the sensors with recyclability is highly desired.

Benefiting from our rational material engineering, all of the sensor ingredients can be fully recycled via an eco-friendly method, as illustrated in Fig. 6a and b. Specifically, the top micro-structured conductive layer and the insulting layer are mainly composed of ethanol-soluble PU (ES-PU) and ethanol-insoluble conductive silver (Ag) paste. Thus, these two layers could be facilely recycled via ethanol dissolution and vacuum filtration. The temperature sensing layers comprising water-soluble PVA and ionic liquid (IL) can be easily extracted and recycled by water. For the final remaining interdigital Ag electrodes on TPU substrate, ethanol-acetone mixture (80%/20% in weight ratio) can be used to swell the TPU substrate and then detach the Ag electrodes from the substrate. The detached Ag paste fragments and the swelled TPU substrate can be easily separated. The collected Ag paste fragments can be dissolved with organic solvent into silver slurry for reuse. In the whole recycling process, no toxic solvents or harsh processes (e.g., high temperature, high pressure, etc.) are involved, exhibiting good recyclability and environmental friendliness.

4. Conclusion

In summary, a new paradigm of intrinsically soft and fully recyclable robotic sensors with quadruple sensing functionalities for safe and reliable HRI has been demonstrated. The integrated quadruple sensing functionalities (i.e., thermal approach sensing, thermal touch sensing, spatial approach sensing, and mechanical force sensing) are realized based on the collaborative design of four different sensing mechanisms, including thermal radiation effect, thermal conduction effect, electric field coupling effect, and capacitor parameter regulation. Enabled by such multifunctionality and versatility, both mechanical and thermal stimulations could be resolved in both contact and non-contact manners. Additionally, the robotic sensors comprise fully recyclable ingredients and can be fully recycled after use, exhibiting superior cost-efficiency and eco-friendliness compared to conventional sensors. As promising applications, a programmable HRI system with diverse functions (including dangerous collision warning, object manipulation monitoring, object recognition and classification, non-contact temperature evaluation, and contact temperature detection) is demonstrated. Nevertheless, there are some limitations for the current version of the sensors. For example, the capacitive signal is not high enough and susceptive to external interference. Besides, simultaneous quadruple sensing has not been achieved. Future work will focus on further optimizing the sensor materials and configuration and developing data acquisition circuits, thus improving the signal robustness and realizing quadruple sensing simultaneously.

Conflict of interest

The authors declare that they have no conflict of interest.

Acknowledgments

Author contributions

Yuexin Cao conducted experiments, analyzed data, and drafted the manuscript. Yuxiang Peng programmed the algorithms, constructed the robot control system, and drafted the manuscript. Wenjuan Ren conducted experiments, analyzed data, drafted the manuscript, and drew relevant conceptual schematics. Honghao Wang participated in part of the experimental processes. Zhimeng Liu and Xin He designed, synthesized, and characterized the polymer materials required for the fabrication of sensors, as well as analyzed data and drafted the manuscript. Yan Diao and Hua Luo provided constructive academic advice and test equipments as well as assisted in manuscript editing. Xiaodong Wu led conceptualization, funding acquisition, and supervision in this study.

Appendix A. Supplementary material

Supplementary data to this article can be found online at https://doi.org/10.1016/j.scib.2025.04.075.

References

[1] Park K, Yuk H, Yang M, et al. A biomimetic elastomeric robot skin using electrical impedance and acoustic tomography for tactile sensing. Sci Robot 2022;7:eabm7187.
[2] Yu Y, Li J, Solomon SA, et al. All-printed soft human-machine interface for robotic physicochemical sensing. Sci Robot 2022;7:abn0495.
[3] Fang H, Wang L, Fu Z, et al. Anatomically designed triboelectric wristbands with adaptive accelerated learning for human–machine interfaces. Adv Sci 2023;10:2205960.
[4] Qiao H, Sun S, Wu P. Non-equilibrium-growing aesthetic ionic skin for fingertip-like strain-undisturbed tactile sensation and texture recognition. Adv Mater 2023;35:2300593.
[5] Yan Y, Hu Z, Yang Z, et al. Soft magnetic skin for super-resolution tactile sensing with force self-decoupling. Sci Robot 2021;6:eabc8801.
[6] Hou B, Yi L, Li C, et al. An interactive mouthguard based on mechanoluminescence-powered optical fibre sensors for bite-controlled device operation. Nat Electron 2022;5:682–93.
[7] Kong Y, Cheng G, Zhang M, et al. Highly efficient recognition of similar objects based on ionic robotic tactile sensors. Sci Bull 2024;69:2089–98.
[8] Jiang Q, Li J, Masood D. Fiber-optic-based force and shape sensing in surgical robots: a review. Sens Rev 2023;43:52–71.
[9] Luo Y, Abidian M, Ahn J, et al. Technology roadmap for flexible sensors. ACS Nano 2023;17:5211–95.
[10] Boutry M, Negre M, Jorda M, et al. A hierarchically patterned, bioinspired e-skin able to detect the direction of applied pressure for robotics. Sci Robot 2018;3:eaau6914.
[11] Wang Y, Adam M, Zhao Y. Machine learning-enhanced flexible mechanical sensing. Nanomicro Lett 2023;15:55.
[12] Chen S, Han X, Hong P, et al. A flexible temperature sensor for noncontact human-machine interaction. Materials 2021;14:7112.
[13] Di Giacomo R, Bonanomi L, et al. Biomimetic temperature-sensing layer for artificial skins. Sci Robot 2017;2:eaai9251.
[14] Zhao D, Zhao L, Wang T, et al. Flexible, conformal composite proximity sensor for detection of conductor and insulator. Chin J Anal Chem 2022;50:20–3.
[15] Wu B, Jiang T, Yu Z, et al. Proximity sensing electronic skin: principles, characteristics, and applications. Adv Sci 2024;11:2308560.
[16] Huang L, Wang S, Zhang K, et al. Research progress of multifunctional flexible proximity sensors. Sens Actuators Phys 2023;360:114500.
[17] Zhang T, Ding Y, Hu C, et al. Self-powered stretchable sensor arrays exhibiting magnetoelasticity for real-time human–machine interaction. Adv Mater 2023;35:2203786.
[18] Wu X, Zhu J, Evans J, et al. A single-mode, self-adapting, and self-powered mechanoreceptor based on a potentiometric–triboelectric hybridized sensing mechanism for resolving complex stimuli. Adv Mater 2021;32:2005970.
[19] Chun S, Kim J, Yoo Y, et al. An artificial neural tactile sensing system. Nat Electron 2021;4:429–38.
[20] Zhu H, Luo H, Cai M, et al. A multifunctional flexible tactile sensor based on resistive effect for simultaneous sensing of pressure and temperature. Adv Sci 2023;11:2307693.
[21] Zhang F, Zang Y, Huang D, et al. Flexible and self-powered temperature–pressure dual-parameter sensors using microstructure-frame-supported organic thermoelectric materials. Nat Commun 2015;6:8356.
[22] Wang H, Chen T, Zhang B, et al. A dual-responsive artificial skin for tactile and touchless interfaces. Small 2025;19:2206830.

[23] Huang J, Wang H, Li J, et al. High-performance flexible capacitive proximity and pressure sensors with spiral electrodes for continuous human–machine interaction. ACS Mater Lett 2022;4:2261–72.

[24] Liu W, Duo Y, Liu J, et al. Touchless interactive teaching of soft robots through flexible bimodal sensory interfaces. Nat Commun 2022;13:5030.

[25] Xiao H, Li S, He Z, et al. Dual mode strain–temperature sensor with high stimuli discriminability and resolution for smart wearables. Adv Funct Mater 2022;33:2214907.

[26] Qiu Y, Wang F, Zhang Z, et al. Quantitative softness and texture bimodal haptic sensors for robotic clinical feature identification and intelligent picking. Sci Adv 2024;10:eadp0348.

[27] Liu Y, Bao R, Tao J, et al. Recent progress in tactile sensors and their applications in intelligent systems. Sci Bull 2020;65:70–88.

[28] Min J, Demchyshyn S, Sempionatto J, et al. An autonomous wearable biosensor powered by a perovskite solar cell. Nat Electron 2023;6:630–41.

[29] Hua Q, Sun J, Liu H, et al. Skin-inspired highly stretchable and conformable matrix networks for multifunctional sensing. Nat Commun 2018;9:244.

[30] Li G, Liu S, Wang L, et al. Skin-inspired quadruple tactile sensors integrated on a robot hand enable object recognition. Sci Robot 2020;5:eabc8134.

[31] Qu X, Xue J, Liu Y, et al. Fingerprint-shaped triboelectric tactile sensor. Nano Energy 2022;98:107324.

[32] Zhang W, Xi Y, Wang E, et al. Self-powered force sensors for multidimensional tactile sensing. ACS Appl Mater Interfaces 2022;14:20122–31.

[33] Mortimer M, Taylor P. Chemical kinetics and mechanism. 1st ed. London: The Royal Society of Chemistry; 2002.